Archives of Materials Science and Engineering

Volume 108
Issue 2
April 2021
Pages 49-67

International Scientific Journal
published monthly by the
World Academy of Materials
and Manufacturing Engineering

DOI: 10.5604/01.3001.0015.0254

The effect of water vapor containing hydrogenous atmospheres on the microstructure and tendency to brittle fracture of anode materials of YSZ–NiO(Ni) system

V.V. Kulyk [a,*], B.D. Vasyliv [b], Z.A. Duriagina [a,c], T.M. Kovbasiuk [a], I.A. Lemishka [a]

[a] Lviv Polytechnic National University, 12 Bandera St., Lviv, 79013, Ukraine
[b] Karpenko Physico-Mechanical Institute of the National Academy of Sciences of Ukraine, 5 Naukova St., Lviv, 79060, Ukraine
[c] The John Paul II Catholic University of Lublin, Al. Racławickie 14, 20-950 Lublin, Poland
* Corresponding e-mail address: kulykvolodymyrvolodymyrovych@gmail.com
ORCID identifier: https://orcid.org/0000-0001-5999-3551 (V.V.K.); https://orcid.org/0000-0002-8827-0747 (B.D.V.); https://orcid.org/0000-0002-2585-3849 (Z.A.D.); https://orcid.org/0000-0003-2792-0555 (T.M.K.); https://orcid.org/0000-0002-3231-0519 (I.A.L.)

ABSTRACT

Purpose: The purpose of this work is to estimate the tendency to brittle fracture of the YSZ–NiO(Ni) anode cermet in a hydrogenous environment with various concentrations of water vapor.

Design/methodology/approach: YSZ–NiO ceramic plates were fabricated by sintering in an argon atmosphere. The treatment of material was performed in a hydrogenous environment with various concentrations of water vapor. The strength test was performed under three-point bending at 20°C in air. The microstructure and morphology of the fracture surface of the specimens were studied using a scanning electron microscope (SEM) Carl Zeiss EVO-40XVP. The chemical composition was determined using an INCA ENERGY 350 spectrometer. Microhardness measurements were performed on a NOVOTEST TC-MKB1 microhardness tester. The configuration of the imprints and cracks formed was studied on an optical microscope Neophot-21. The porosity of the materials was investigated by analysing the SEM micrographs using the image processing technique.

Findings: Peculiarities of changes in the microstructure, the morphology of specimens fracture surface, physical and mechanical characteristics of YSZ–NiO(Ni) material for solid oxide fuel cell (SOFC) anodes of different preconditioning modes aged under various partial pressures of water vapor in a hydrogenous environment are found.

Research limitations/implications: To study the actual behaviour of the YSZ–NiO(Ni) anode material in the operating environment, it is necessary to evaluate its strength, Young's modulus, microhardness, and fracture toughness by changing with a certain step the partial pressure of water vapor in the whole range noted in this work.

© Copyright by International OCSCO World Press. All rights reserved. 2021

Practical implications: Based on the developed approach to assessing the propensity to brittle fracture of the formed cermet microstructure, it is possible to obtain an anode material that will provide the necessary functional properties of a SOFC.

Originality/value: An approach to estimating the propensity to brittle fracture of a formed cermet structure is proposed based on the microhardness and fracture toughness characteristics obtained by the Vickers indentation method.

Keywords: YSZ–NiO ceramics, Hydrogen, Water vapor, Microhardness, Fracture toughness, Microstructure and fracture mechanism

Reference to this paper should be given in the following way:

V.V. Kulyk, B.D. Vasyliv, Z.A. Duriagina, T.M. Kovbasiuk, I.A. Lemishka, The effect of water vapor containing hydrogenous atmospheres on the microstructure and tendency to brittle fracture of anode materials of YSZ–NiO(Ni) system, Archives of Materials Science and Engineering 108/2 (2021) 49-67. DOI: https://doi.org/10.5604/01.3001.0015.0254

MATERIALS

1. Introduction

Nowadays, there are many types of energy sources for individual and industrial applications. Among them, environmentally friendly fuel cell technology is promising from the point of view of prevention of air, water, and earth's surface pollution [1,2]. The key position among fuel cells as electrochemical devices for direct conversion of chemical energy into electricity is occupied by solid oxide fuel cells (SOFCs) [3].

A nickel cermet based on yttria-stabilized zirconia (YSZ–Ni) is most often used for SOFC anodes in cases of operating in hydrogen-containing gas mixtures, since it is characterized by a coefficient of thermal expansion close to electrolytes based on ZrO_2, improved catalytic activity during hydrogen oxidation, and structural stability when operating in a hydrogen-containing environment [3-6].

Based on theoretical models of the interaction of the operating environment of a SOFC with materials of electrodes in the zone of the fuel oxidation reaction [5,7,8] and the results of calculations [9-12], it is concluded that the main action of the environment occurs at triple phase boundaries and these phases are nickel and zirconium phases, as well as a virtual "porosity" phase for transporting fuel molecules or reaction products. The concentration of hydrogen in the operating environment plays a key role in the passage of such a reaction. Accordingly, the amount and pressure of water vapor, both present in the environment and formed in the reaction, affect the structural integrity of SOFC components, especially in the zone of the fuel oxidation reaction [9,13].

The startup of a newly created SOFC begins with the stage of NiO to Ni reduction in sintered YSZ–NiO anodes to form an electrically conductive nickel network in the anode [3]. It is important to form a perfect structure of the YSZ–Ni cermet, resistant to degradation under operating conditions [13,14]. In the works [15,16] the technology of reduction-oxidation (redox) cycling of the YSZ–NiO anode material was developed, and the mode of its treatment for five cycles in a hydrogen-containing gas mixture and air at 600°C with final one-time reduction was proposed. As a result of this treatment, a cermet was obtained, which had a significant advantage in strength and electrical conductivity over the one-time reduced material. At present, the industrial implementation of this treatment is promising, but it is necessary to verify the effectiveness of its application for conditions involving a certain concentration of water vapor in the hydrogen-containing gas mixture. Therefore, the development of a method of structural optimization, which will provide the required structural and functional properties of materials for SOFC anodes, is an urgent and necessary task to be solved.

The strength of the materials from which SOFC anodes are made is traditionally the main property used for assessing the bearing capacity of anodes [17-19]. However, one of the key functional requirements for the SOFC anodes is high porosity to ensure the supply of fuel to the zone of its oxidation reaction [3,18]. Due to this microstructural feature of the anode, the strength may be an insufficient characteristic of its bearing capacity. Among the methods of fracture mechanics, there are more structurally sensitive ones, which allow assessing the propensity of such porous material to the initiation of microcracks and the ability to resist their propagation, because such microcracks can lead to the failure of the anode and the entire SOFC. Therefore, it is advisable to study the behaviour of YSZ–NiO ceramics in the as-sintered state and corresponding cermets reduced in different modes, in particular their microstructure and propensity to brittle fracture under model operation conditions (aging) in a hydrogen-containing gas mixture with water vapor of various concentrations.

The indentation method is one of the first and most common mechanical methods for diagnosing the load-bearing capacity of ceramic materials and products. Conditions for measuring the microhardness of materials are regulated by the relevant standards [20,21].

An important aspect of the mechanical behaviour of ceramic materials is their tendency to brittle fracture due to the formation and growth of cracks [22,23]. This property of the material, namely the fracture toughness, is evaluated by calculating the critical stress intensity factor K_{Ic}. Scientific groups of researchers have long proposed the use of methods for estimating the fracture toughness of brittle material in terms of indentation by the Vickers pyramid, thoroughly described and confirmed by analytical calculations and experiments [24-38]. Formulas (1-9), given in Table 1, represent a segment of research concerning the assessment of the fracture toughness of brittle ceramic materials by the indentation method. These formulas comprise physical and mechanical parameters, as well as empirical coefficients. Therefore, some of the formulas can only be used to assess the fracture toughness of a narrow range of ceramic materials. In some formulas (see Tab. 1) both Young's modulus and microhardness appear, while in others one or more parameters may be absent. Some of the given formulas are similar but differ by experimentally determined coefficients. A large number of empirically determined powers for the corresponding power functions of relevant material characteristics in some formulas may be the reason for the low accuracy of the calculated values of fracture toughness, which limits the use of these formulas.

Table 1.
Formulas for estimating the fracture toughness of brittle ceramic materials, according to references [24-38], and corresponding parameters for calculations

Formulas for estimating the fracture toughness of brittle ceramic materials	Units	Units for corresponding parameter in formulas					Formula No.	Reference No.
		indentation load P	microhardness H	Young's modulus E	radial crack length c	length of the imprint half diagonal a		
$K_{Ic} = 0.0177\left(\frac{HP}{c}\right)^{1/2}$ (for SiC) or $K_{Ic} = 0.0154\left(\frac{HP}{c}\right)^{1/2}$ (Al_2O_3)	$MPa \cdot m^{1/2}$	kg	kgf/mm^2	–	mm	–	(1)	[24]
$K_{Ic} = 0.0726\left(\frac{P}{c^{3/2}}\right)$	$Pa \cdot m^{1/2}$	N	–	–	m	–	(2)	[25]
$K_{Ic} = 0.0752\left(\frac{P}{c^{3/2}}\right)$	$Pa \cdot m^{1/2}$	N	–	–	m	–	(3)	[26]
$K_{Ic} = 0.0725\left(\frac{P}{c^{3/2}}\right)$	$Pa \cdot m^{1/2}$	N	–	–	m	–	(4)	[27]
$K_{Ic} = \frac{0.0424(PE/a)^{0.5}}{(c/a)^{1.57}}$	$MPa \cdot m^{1/2}$	N	–	GPa	mm	mm	(5)	[28,29]
$K_{Ic} = 0.016\left(\frac{E}{H}\right)^{1/2}\left(\frac{P}{c^{3/2}}\right)$	$Pa \cdot m^{1/2}$	N	GPa	GPa	m	–	(6)	[35]
$K_{Ic} = 0.014\left(\frac{E}{H}\right)^{1/2}\left(\frac{P}{c^{3/2}}\right)$	$Pa \cdot m^{1/2}$	N	GPa	GPa	m	–	(7)	[36]
$K_{Ic} = 0.0285 H^{0.6} E^{0.4} a^{0.5} \ln\left(\frac{8.4a}{c}\right)$	$MPa \cdot m^{1/2}$	–	MPa	MPa	m	m	(8)	[37]
$K_{Ic} = 0.0735 H^{0.6} E^{0.4} a^{0.5} \left(\frac{c}{a}\right)^{-0.56}$	$MPa \cdot m^{1/2}$	–	MPa	MPa	m	m	(9)	[38]

To obtain reliable values of the fracture toughness of the investigated material by the indentation method, they must be compared with those obtained for such material by traditional methods of fracture mechanics. In the work [39], the K_{Ic} values were calculated according to each of the formulas proposed above (Tab. 1) for ZrO_2–Y_2O_3 model ceramics. These values were further compared with those obtained for such material by traditional methods of fracture mechanics. Based on such studies, formula (6) was substantiated and selected as the optimal one among the given formulas (Tab. 1) for the characterization of YSZ–NiO anode ceramics and the corresponding cermets [39].

Therefore, in this study, we considered it appropriate to use the indentation method with the calculation of the critical stress intensity factor K_{Ic} by formula (6).

This work aims to estimate the tendency to brittle fracture of the YSZ–NiO(Ni) anode cermet preconditioned in different modes (as-sintered – no preconditioning; one-time reduced in Ar–5 vol% H_2 mixture; redox treated for five cycles in Ar–5 vol% H_2 mixture and air with the final reduction in Ar–5 vol% H_2 mixture) after aging in a hydrogenous environment with various concentrations of water vapor by detecting changes in microstructure, phase composition, and fracture toughness.

2. Experimental procedures

Ceramics of the YSZ–NiO system (zirconium oxide, stabilized by 8 mol% Y_2O_3, with the addition of 50 wt% NiO; hereinafter – YSZ–NiO) were investigated. The nickel phase of the ceramics undergoes reduction in a high-temperature hydrogenous environment after sintering to acquire the necessary functional properties. In recent decades, a cermet formed in this way is perhaps the most common modern material for SOFC anodes [3,13].

NiO starting powders with initial particle sizes of 0.90…0.96 μm and YSZ with initial particle sizes of 0.10…0.15 μm were used. Powders YSZ and NiO were mixed in a drum mill using grinding bodies of zirconia ceramics in isopropyl alcohol. In addition to the mixture of 8YSZ–NiO powders, the slurry contained the following components: ethylcellulose (polymer); dibutyl phthalate (plasticizer); isopropyl alcohol (solvent). Plates of YSZ–NiO ceramics were made by three-dimensional (3D) printing and preliminary (at 700°C for 2 h) and final sintering (at 1450°C for 2 h) in an argon atmosphere, which ensured the grain size of the ceramics in the range of 1-2 μm [6,40,41].

Seven variants of the material were studied (Tab. 2): (1) ceramics in the as-sintered state [39]; (2) as-sintered ceramics, aged under conditions where the partial pressure of water vapor (pH_2O) was 3.0×10^4 Pa; (3) as-sintered ceramics, aged at pH_2O of 1.48×10^5 Pa; (4) one-time reduced cermet, aged at pH_2O of 3.0×10^4 Pa; (5) one-time reduced cermet, aged at pH_2O of 1.48×10^5 Pa; (6) treated by redox (reduction/oxidation) cycling cermet, aged at pH_2O of 3.0×10^4 Pa; (7) treated by redox cycling cermet, aged at pH_2O of 1.48×10^5 Pa. The aging experiment was performed in a hermetic chamber under a constant pressure of water vapor (see Tab. 2) balanced with Ar–5 vol% H_2 at 600°C for 4 h.

Table 2.
Influence of treatment modes on physical and mechanical properties of investigated materials [39]

Variant	Preconditioning mode	Aging at pH_2O, MPa	The average value of the characteristics					
			σ_f, MPa	σ_f/σ_{f0}, %	E/E_0, %	E, GPa	σ, S/m	Porosity, %
1	As-sintered ceramics	No aging	112	100	100	150	(*)	25.2
2	As-sintered ceramics	0.030	91	81	83.7	126	8.4×10^4	25.9
3		0.148	113	101	97.0	146	2.1×10^{-4}	25.4
4	One-time reduction in Ar–5 vol% H_2 at 600°C for 4 h, p=0.15 MPa	0.030	95	85	80.1	120	4.3×10^5	26.5
5		0.148	82	73	80.8	121	3.2×10^5	18.1
6	Redox treatment in Ar–5 vol% H_2/air at 600°C for 5 cycles followed by one-time reduction in Ar–5 vol% H_2 at 600°C for 4 h, p=0.15 MPa	0.030	98	88	81.2	122	3.4×10^5	18.0
7		0.148	75	67	72.0	108	2.9×10^5	19.0

Note: σ_f is the ultimate bend stress; σ_f/σ_{f0} is the relative strength; E is Young's modulus; E/E_0 is the relative stiffness (a ratio of Young's modulus for material after treatment E to that for material in the as-sintered state E_0); σ is the specific electrical conductivity.
(*) The electrical conductivity is very low.

One-time reduction of prismatic specimens was carried out in a sealed chamber with an electric resistance furnace in the following mode: heating in vacuum up to 600°C, holding for 4 h in Ar–5 vol% H_2 mixture under a pressure of 0.15 MPa and cooling in argon [15,16,42]. Redox treatment of prismatic specimens was carried out according to the developed method [15,16,42]: heating in vacuum to 600°C, holding for 4 h in Ar–5 vol% H_2 mixture under a pressure of 0.15 MPa, evacuation of the test chamber, oxidation of specimens in air for 4 h at 600°C and cooling in air. Five treatment cycles were performed according to this scheme. The last stage of treatment after redox cycling was the reduction of the material in a hydrogenous environment and cooling in argon. The heating/cooling rate was 20°C/min [15,16].

Mechanical tests of the material under three-point bending [39] were performed on the MTS Criterion E43.104 test machine at 20°C in air. Appropriate formulas were used for calculations [43,44]. According to the obtained stress–flexure diagrams, the fracture stresses for ceramics in the as-sintered state (σ_{f0}) and after treatment (σ_f) were determined. Five specimens of each of the investigated material variants were tested and the mean fracture stress was calculated. The relative strength of the material was defined as the σ_f / σ_{f0} ratio [43]. For further analysis, we chose that diagram in the coordinates of "stress–flexure", where the obtained value of the fracture stress for a certain material variant was closest to the calculated average value. Selected for each variant of the material (Tab. 2) stress–flexure diagrams (Fig. 1) were used to calculate Young's modules according to the previously proposed method [43] on the basis of the corresponding slopes of the diagrams. The Young's modulus of YSZ–NiO ceramics in the as-sintered state E=150 GPa was determined on the basis of the analysis of literature sources [17,18]. The Young's modules for the investigated material variants were calculated by the formula:

$$E_i = \frac{\sigma_i}{\sigma_0} \cdot E_0 \qquad (10)$$

where E_i and σ_i are Young's modulus and stress in the material, respectively, after appropriate treatment at a certain level of flexure δ=const, selected within the section of elastic deformation under bending, E_0 and σ_0 are Young's modulus and stress in the material, respectively, in the as-sintered state at the same level of deformation.

The microhardness of the studied material variants was measured using a NOVOTEST TC-MKB1 microhardness tester at six levels of indentation load: 0.49 N, 0.98 N, 1.96 N, 2.94 N, 4.91 N, and 9.81 N. According to the standards, the hardness is determined by the size of the imprint left by the Vickers indenter on the surface of the specimen [20,21]. The microhardness tester allows you to automatically apply a load to the indenter and provides exposition for 10-15 sec. After entering the values of the optically measured diagonals of the imprint, the microhardness tester automatically calculates the arithmetic mean of the imprint diagonal length and then calculates the value of microhardness as the ratio of the load applied to the indenter to the inclined surface area of the imprint.

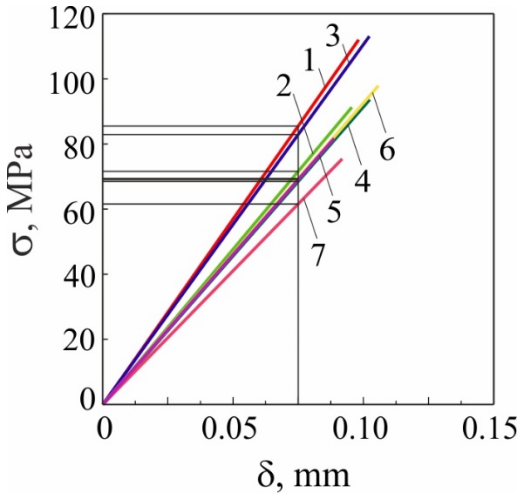

Fig. 1. Stress–flexure diagrams of material of variants 1-7 (Tab. 1) [39]

The microhardness of each material variant (Tab. 2) was determined by making at least 10 indentations for each of the selected load levels. According to ASTM C 1327 [21], the obtained values (in kgf/mm^2) were converted into other units of measurement (GPa).

To assess the fracture toughness of the material under Vickers pyramid indentation conditions, we used an array of force (microhardness, indentation load, and Young's modulus) and geometric (indentation diagonal length 2a, angular crack length l, and total crack length c (if any) according to ASTM C 1327 [21]) parameters. The fracture toughness values were calculated by the formula (6).

Microstructure and fracture surface morphology of specimens tested were studied using a scanning electron microscope (SEM) Carl Zeiss EVO-40XVP. An INCA ENERGY 350 spectrometer with an energy dispersive X-ray (EDX) microanalysis was used to determine the chemical composition of the material in local areas. An optical microscope Neophot-21 was used to study the geometry of imprints and cracks that appeared in the material.

The porosity of the materials was determined by the hydrostatic weighing method. We also used the express method of determining porosity successfully tested by the

authors of the works [45,46] by analysing SEM images of the material microstructure [47]. This allowed clarifying the obtained values.

The specific electrical conductivity was measured in air at 20°C using a four-probe method described elsewhere [16,39].

3. Results and discussion

3.1. Reduction/oxidation stability conditions

For each of the studied aging regimes, it was important to determine the oxygen partial pressure (pO_2) to establish the conditions for the reduction and oxidation of the phases present in the material modifications. That is, we intended to investigate the behaviour of the material, taking into account the Ellingham diagrams (stability lines for Ni/NiO, Zr/ZrO_2, and Y/Y_2O_3). It is known that when this pO_2 becomes too low for a certain oxide phase, it might start to reduce. Conversely, when the pO_2 becomes too high for a certain metallic (non-oxidized) phase, it might start to oxidize. Such changes can affect the entire reduction-oxidation process. It was determined according to the Ellingham diagram [48] for the Ni/NiO stability line (curve 1 in Fig. 2), that the equilibrium partial pressure of oxygen at 600°C is 3.0×10^{-16} Pa (curve 5 in Fig. 2). Also, using method [9], the pO_2 was calculated for the conditions when the values of the water vapor partial pressure (pH_2O) were 3.0×10^4 Pa and 1.48×10^5 Pa. The calculated values of pO_2 were 5.0×10^{-20} Pa and 6.6×10^{-15} Pa (curves 8 and 9 in Fig. 2), respectively.

Since the calculated pO_2 value at $pH_2O = 3.0\times10^4$ Pa (curve 8 in Fig. 2) is much lower than the equilibrium oxygen partial pressure (curve 5 in Fig. 2) for the Ni/NiO stability line, NiO can be reduced under these conditions. For the Zr/ZrO_2 stability line (curve 2 in Fig. 2) it was found that the equilibrium partial pressure of oxygen at 600°C is 10^{-50} Pa. This value is significantly lower than the calculated pO_2 value at $pH_2O = 3.0\times10^4$ Pa. Therefore, this mode provides stable conditions for the ZrO_2 phase in the oxidized state. Similarly, it was found for the Y/Y_2O_3 stability line (curve 3 in Fig. 2) that the equilibrium partial pressure of oxygen at 600°C is 10^{-60} Pa. This value is significantly lower than the calculated pO_2 value at $pH_2O = 3.0\times10^4$ Pa and even lower than the equilibrium partial pressure of oxygen determined for the Zr/ZrO_2 stability line. Therefore, as for ZrO_2, this mode provides stable conditions for the Y_2O_3 phase in the oxidized state. Thus, at $pH_2O = 3.0\times10^4$ Pa, only the NiO phase can be reduced.

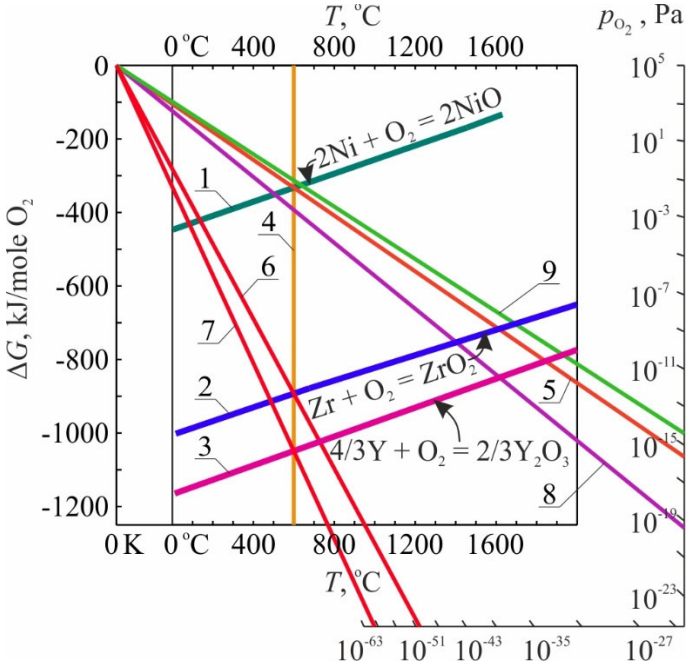

Fig. 2. Schematic of determining the state of the material in environments with various partial pressure of oxygen pO_2 based on the Ellingham diagrams [48] for the stability of Ni/NiO, Zr/ZrO_2, and Y/Y_2O_3 (lines 1-3, respectively): for the position of 600°C marked with vertical line 4, lines 5-7 show corresponding values of the equilibrium partial pressure of oxygen on the pO_2 scale for these conditions; line 8 shows the value of pO_2 for the partial pressure of water vapor 0.03 MPa, and line 9 shows the value for 0.148 MPa

At $pH_2O = 1.48\times10^5$ Pa, the calculated pO_2 value (curve 9 in Fig. 2) was higher than the equilibrium oxygen partial pressure (curve 5 in Fig. 2) for the Ni/NiO stability line. Such conditions contribute to the oxidation of the metallic (non-oxidized) nickel phase. According to the Zr/ZrO_2 and Y/Y_2O_3 stability lines and corresponding values of the equilibrium partial pressure of oxygen at 600°C (10^{-50} Pa and 10^{-60} Pa, respectively), this mode provides stable conditions for both the ZrO_2 and Y_2O_3 phases in the oxidized state, even better than at $pH_2O = 3.0\times10^4$ Pa. Thus, at $pH_2O = 1.48\times10^5$ Pa, no phase can be reduced.

3.2. Mechanical properties and the microstructural aspect

In the work [39], it was noted that for ZrO_2–Y_2O_3 ceramics (zirconium oxide stabilized by 8 mol% Y_2O_3) it is possible to obtain invariant values of microhardness and fracture toughness in a certain range of indentation load. For this material, microhardness data set under the indentation loads of 0.49 N, 0.98 N, 1.96 N, 2.94 N, 4.91 N, and 9.81 N was obtained and a regression function was fitted to the data. This function indicates the dependence of the microhardness of the material on the load, known as the indentation size effect [49-51]. This effect is a decrease in the average values of microhardness with increasing indentation load. For the studied material, the microhardness versus load dependence reaches the plateau at indentation loads from 4.91 N to 9.81 N (the latter value was the upper limit of the microhardness tester).

For the as-sintered YSZ–NiO ceramics and the reduced YSZ–NiO(Ni) cermet, invariant values of microhardness and fracture toughness in the specified load range were also obtained [39]. The microstructure of their YSZ ceramic skeleton is similar in nature to ZrO_2–Y_2O_3 ceramics [52].

According to the results of microhardness measurements for the YSZ–NiO(Ni) cermet variants studied in the present work under the indentation loads of 0.49 N, 0.98 N, 1.96 N, 2.94 N, 4.91 N, and 9.81 N, dependences were obtained (Fig. 3a), of which 1, 2, 3, and 5 are similar to the above-mentioned ones exhibiting a decrease in the average values of microhardness with increasing indentation load. In dependences 4, 6, and 7, on the contrary, the values of microhardness are minimal under the lowest load, which is not typical of ceramics. However, for all dependences, the yield of average values on the plateau at indentation loads from 4.91 N to 9.81 N was observed.

In the work [39], the values of the fracture toughness K_{Ic} for ZrO_2–Y_2O_3 ceramics were calculated by formulas (1-9) given in Table 1. Since the values of the fracture toughness determined by the Vickers indentation method using formula (6) are closest to those obtained by other fracture mechanics methods, it has been proposed to use this formula as the most optimal. Since the same formula is recommended for use by other researchers [34,53,54], it was used in the present work to assess the crack growth resistance of the studied variants of the YSZ–NiO(Ni) cermet and to compare the results with those obtained for the same cermet in the work [39].

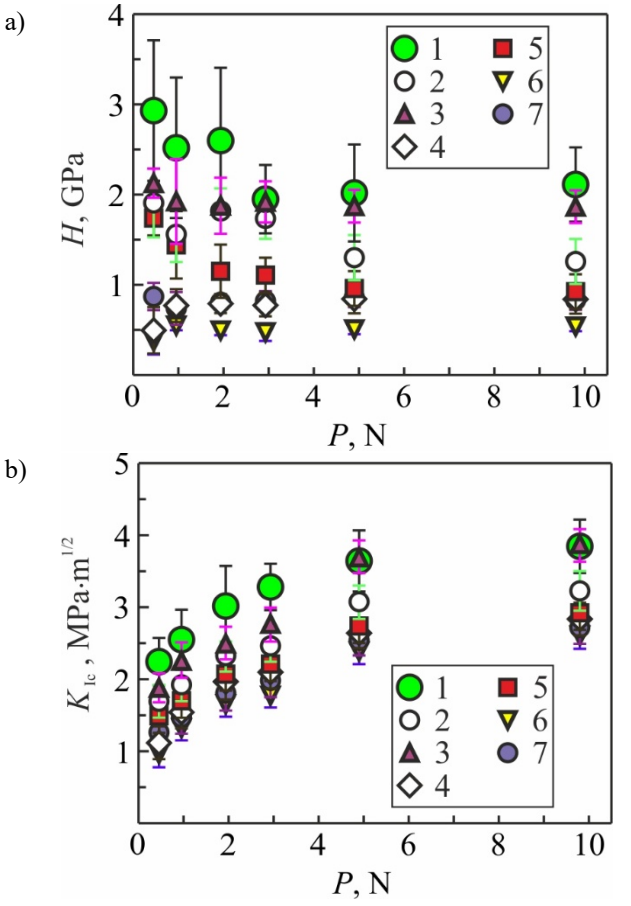

Fig. 3. Change of mechanical characteristics of the investigated materials of variants 1-7 under Vickers pyramid indentation conditions depending on the indentation load: Vickers microhardness (a); fracture toughness (b)

The values of fracture toughness (in MPa·m$^{1/2}$) of materials of variants 1-7 were calculated for each level of indentation load P and the corresponding value of microhardness H [35]. For all investigated variants of the material, we notice a similarity to the given in the work [35] trend of increasing K_{Ic} values with increasing indentation load, and the values reach the plateau at indentation loads from 4.91 N to 9.81 N (Fig. 3b). Therefore, to compare the

mechanical properties of materials of various variants, in addition to the average values of Young's modulus and flexural strength (Fig. 4a), we used further the values of fracture toughness and microhardness obtained in the range of indentation load 4.91-9.81 N (Fig. 4b).

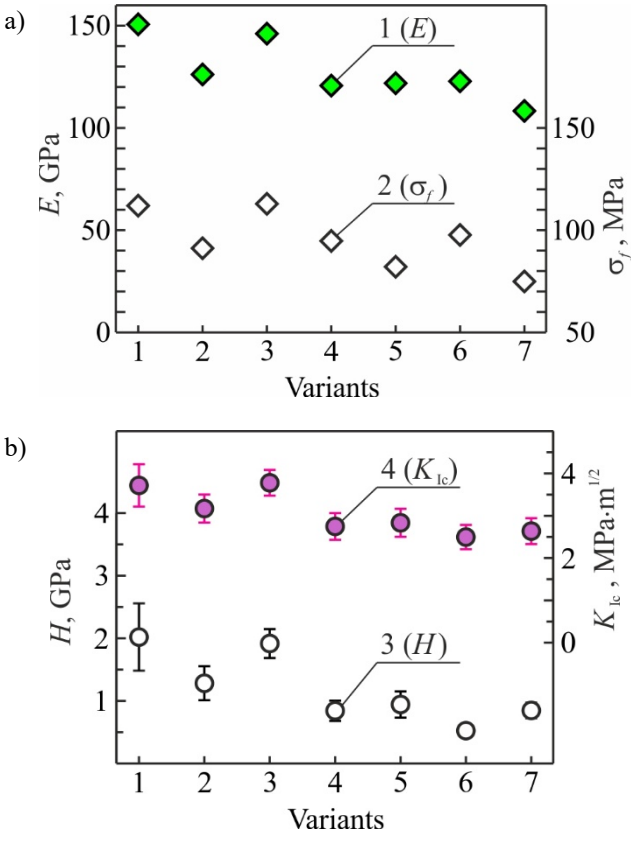

Fig. 4. Mechanical characteristics of the investigated materials of variants 1-7: the average values of Young's modulus (dependence 1) and bend strength (dependence 2) (a); Vickers microhardness (dependence 3) and fracture toughness (dependence 4) under the indentation load in the range of 4.91 to 9.81 N (b)

Based on Ellingham diagrams (Fig. 2), we have determined the conditions for the reduction and oxidation of the phases present in the as-sintered ceramics and cermet, and on their basis, we can explain different mechanical behaviors of the studied material variants. Thus, the effect of water vapor admixture in a hydrogenous environment on the as-sintered ceramics can be traced in variants 2 and 3 (Tab. 2). Lower by 16.3% and 19% levels of Young's modulus and strength (Tab. 2, Fig. 4a), as well as significantly lower fracture toughness and microhardness (Fig. 4b) of the material of variant 2 aged in a water vapor-depleted environment ($pH_2O = 3.0\times10^4$ Pa), compared to the material in the as-sintered state (variant 1, Tab. 2, Fig. 4), are consistent with the statement on the possible reduction of the NiO phase under these conditions and confirmed by the results of SEM analysis.

In contrast to the fracture along the boundaries of the agglomerates, which unite several NiO phase particles around the fragments of the ceramic YSZ skeleton (Fig. 5a), and the presence of individual facets of the transgranular cleavage (Fig. 5b) on the specimen fracture surface of variant 1, SEM images of the specimen fracture surface of variant 2 exhibit both signs of transgranular fracture and several microregions of plastically elongated metallic nickel from the fringes formed on the surfaces of NiO particles (Fig. 5c, d). The thin fringes of the reduced nickel resulted in the loss of interparticle bonds due to its shrinkage in nanovolumes and the appearance of microcracks along the boundaries between particles, which are commensurate with the size of the nickel phase particles (Fig. 5d). The material has become electrically conductive, but the level of electrical conductivity (Tab. 2) is still too low for SOFC anodes [3,15,18].

The strength of the material of variant 3, aged in a water vapor-enriched environment ($pH_2O = 1.48\times10^5$ Pa), did not change compared to the as-sintered ceramics, and Young's modulus of this material decreased slightly (Table 2, Fig. 4a). The fracture toughness remained the same and the microhardness decreased slightly (Fig. 4b). No visible signs of degradation of the microstructure of this material were detected, and the fracture is dominated by cleavage facets of NiO and YSZ particles located at the agglomerate boundaries while maintaining the integrity of these agglomerates (Fig. 5e, f). This change in the fracture micro-mechanism together with a slight decrease in Young's modulus while maintaining levels of strength (Fig. 4a), microhardness, and fracture toughness at a significant reduction in scatter bands in the material test data (Fig. 4b) were probably caused by water vapor assisted lowering of residual stresses in YSZ–NiO ceramics [25,26, 55-58]. The electrical conductivity of the material is very low (Tab. 2).

The effect of a water vapor admixture in the hydrogenous environment on the one-time reduced YSZ–NiO(Ni) cermet can be traced in variants 4 and 5 (Tab. 2), taking into account the conditions determined on the basis of Ellingham diagrams (Fig. 2) for reduction and oxidation of phases available in this cermet, as well as patterns of behaviour of the material in these conditions, noted in the works [4,5,7]. Certain levels of physical and mechanical characteristics may be in favour of considerations for additional reduction of the NiO phase in the material of variant 4, aged in a water vapor-depleted environment

(pH_2O = 3.0×10^4 Pa). Young's modulus, strength, fracture toughness, and microhardness of this material are lower by 19.9%, 15.0%, 26.7%, and 57.5%, respectively (Table 2, Fig. 4a, b), compared to the as-sintered ceramics (variant 1).

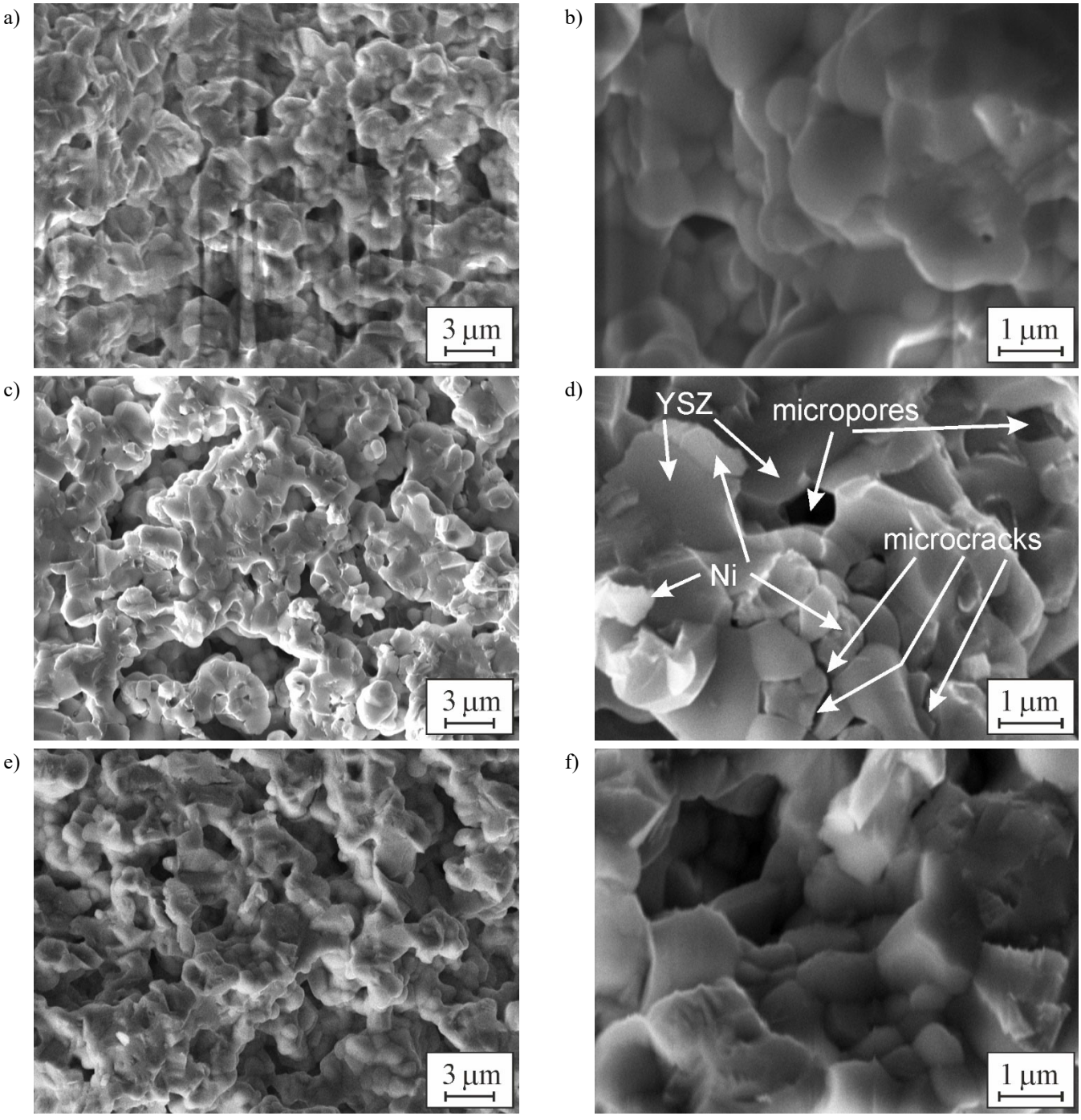

Fig. 5. SEM fractography (SE images) of specimens (a, b) in the as-sintered state (variant 1) and aged in (c, d) water vapor-depleted Ar–5 vol% H_2 mixture (variant 2, water vapor partial pressure 0.03 MPa) and in (e, f) water vapor-enriched Ar–5 vol% H_2 mixture (variant 3, water vapor partial pressure 0.148 MPa), at (a, c, e) low and (b, d, f) high magnifications. The arrows (d) denote microcracks along the boundaries between NiO(Ni) and YSZ particles

This mechanical behaviour of the material is consistent with the results of SEM analysis. Thus, the YSZ–NiO(Ni) cermet preconditioned with one-time reduction shows a relatively homogeneous microstructure with uniformly distributed isolated pores of sizes in the range of 2-10 μm (Fig. 6a, b), as noted in the work [39].

It is known [18] that the initiation and propagation of microcracks in reduced cermets are influenced by the morphology of pores and their size. The pores serve as potential foci of microcracks. In addition to the observed large pores at low magnifications of the microscope (Fig. 6a), smaller interparticle pores 0.2-1.5 μm in size were

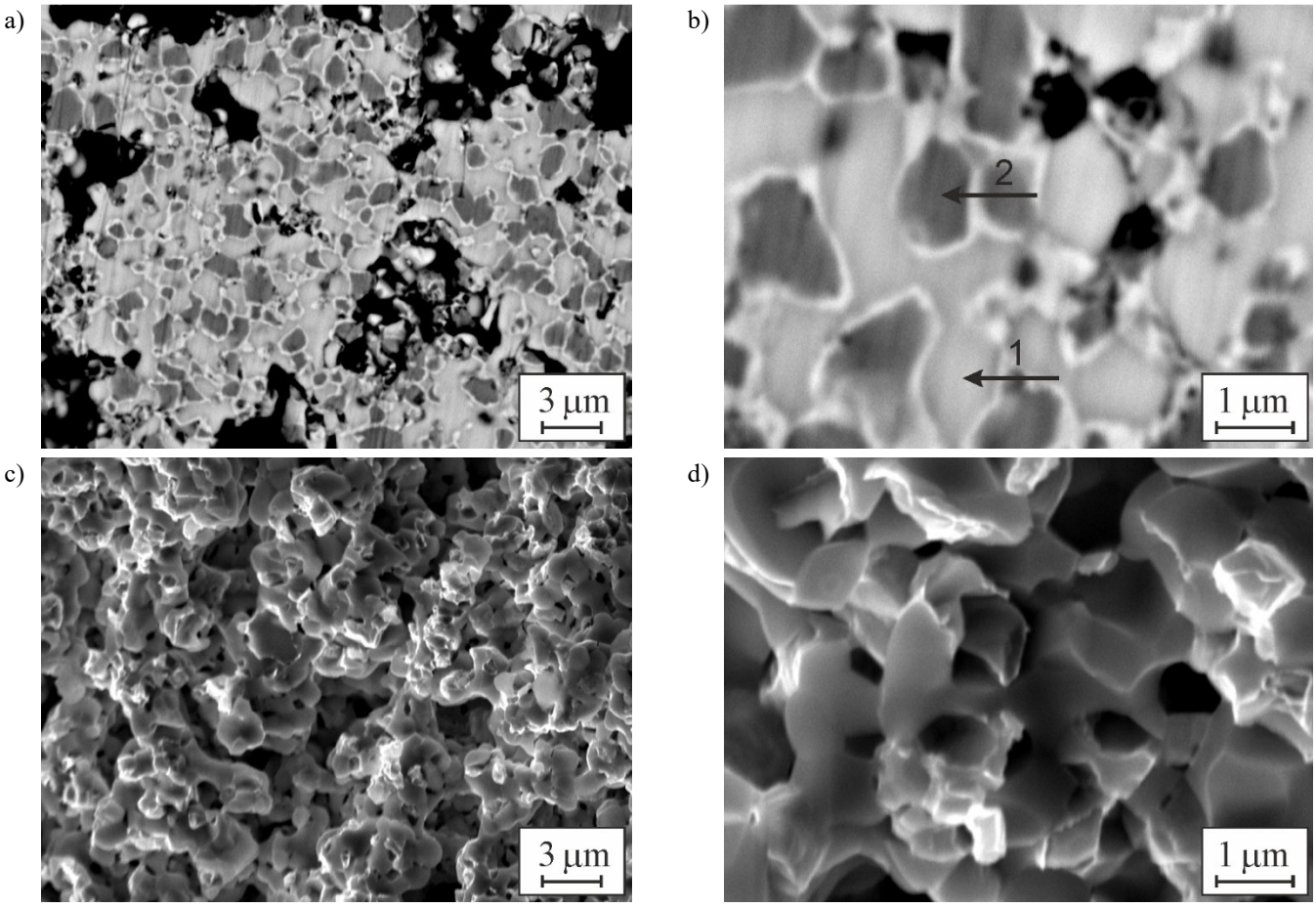

Fig. 6. SEM (a, b) microstructures (BSD images) and (c, d) fractography (SE images) of specimens preconditioned by one-time reduction in Ar–5 vol% H_2 mixture, at (a, c) low and (b, d) high magnifications. Black numbered arrows indicate EDX analysis areas (see Tab. 3)

Table 3.
Data of EDX spectra 1 and 2 of the YSZ–NiO(Ni) cermet specimen preconditioned with one-time reduction. The spectra correspond to areas 1 and 2, indicated by black numbered arrows in Fig. 6b

Chemical element and X-ray series	Spectrum 1		Spectrum 2	
	wt.%	at%	wt.%	at%
O K	19.09	57.30	18.47	49.73
Ni K	–	–	44.80	32.88
Y L	6.14	3.32	3.52	1.71
Zr L	74.77	39.38	33.21	15.68

found in this cermet (Fig. 6b). Light grey areas in Fig. 6b (see zone 1; Tab. 3, spectrum 1) is a ceramic matrix of zirconium dioxide. The grains of the nickel phase in the form of dark grey areas, each of which is bounded by a white fringe (zone 2 in Fig. 6b; Tab. 3, spectrum 2), are evenly distributed in this matrix. The white fringes are metallic Ni that surrounds the dark grey areas of NiO. On the fracture surface of the specimen of this cermet, microregions of elongated metallic nickel (up to 1 μm^2) are uniformly distributed (Fig. 6c, d). The intergranular fracture micromechanism which is characteristic of one-time reduced Ni-containing anode materials [3,18,30] dominates here.

The material of variant 4 was obtained due to the aging of the one-time reduced cermet in a water vapor-depleted environment (pH_2O = 3.0×10^4 Pa). It is characterized by thicker fringes on the nickel phase particles (Fig. 7a, b) and has a satisfactory electrical conductivity (Tab. 2), which indicates an additional reduction of NiO [5,12,55]. Similar to the behaviour of one-time reduced material before aging, a predominance of the intergranular fracture micromechanism with uniformly distributed ridges of elongated metallic nickel was revealed on the specimen fracture surface of this cermet (Fig. 7c, d).

The strength of the one-time reduced cermet after aging in an environment with a high content of water vapor (variant 5) decreased by 27% compared to the as-sintered ceramics, whereas Young's modulus of this material decreased only by 19.2% approaching the levels of variants 2 and 4 (Tab. 2, Fig. 4a). This atypical decrease in cermet strength is probably due to its reoxidation in a water vapor-enriched atmosphere [11,12]. This explanation is supported by slightly higher values of microhardness and fracture toughness of this cermet (Fig. 4b) compared to those for cermet aged in a water vapor-depleted environment (variant 4), as well as the observed microstructural changes in the form of swelling of the fringes with the formation of porous

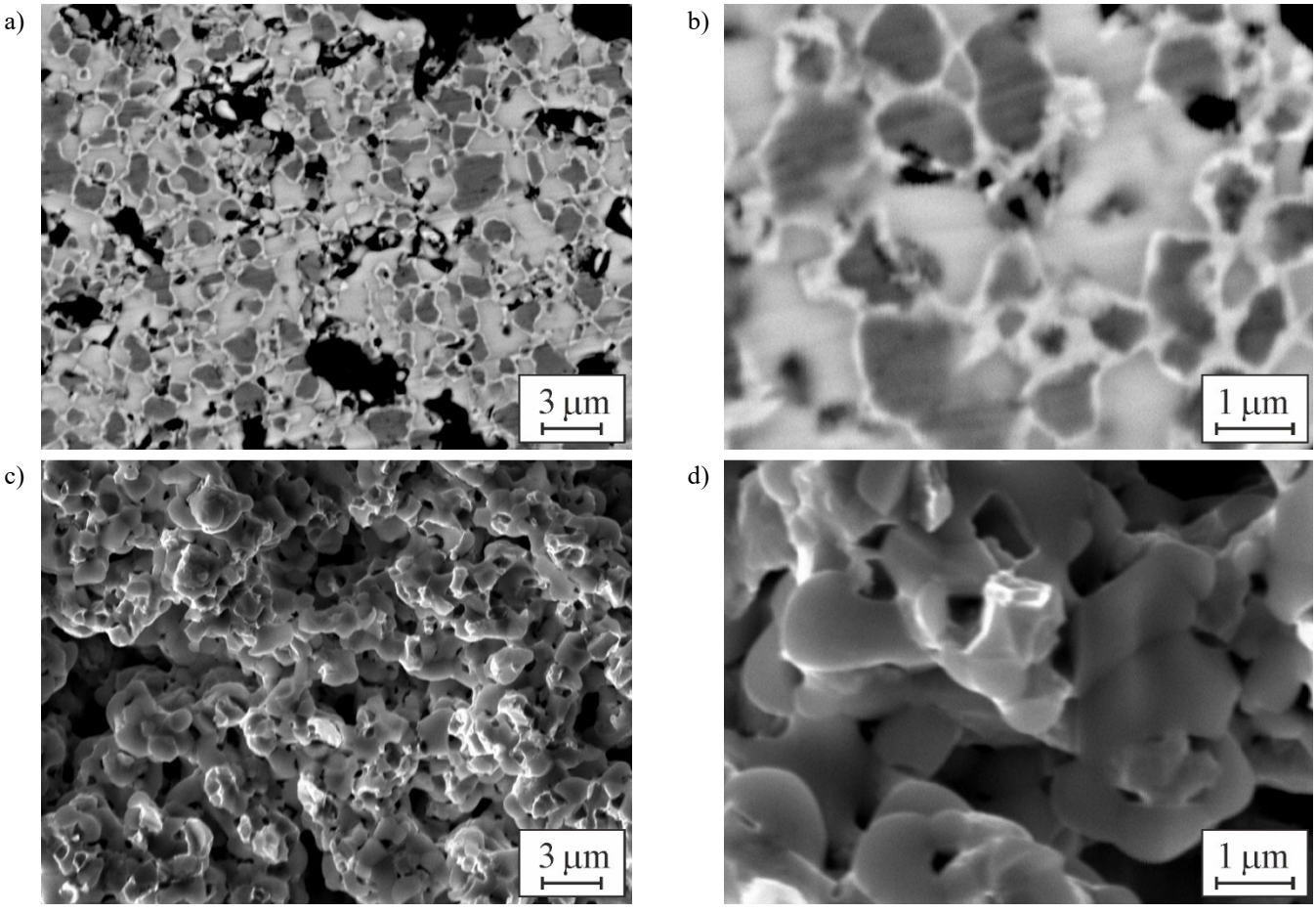

Fig. 7. SEM (a, b) microstructures (BSD images) and (c, d) fractography (SE images) of the material of variant 4 at (a, c) low and (b, d) high magnifications

NiO nanofilms (Fig. 8a, b). This is evidenced by the light areas of nickel oxide on the fracture surface, which have rounded edges (Fig. 8c, d), and a significant reduction in porosity (Tab. 2). The electrical conductivity of the cermet decreased slightly (Tab. 2). Here we also observe the intergranular fracture micromechanism due to the weakening of the cohesive strength of the bond between the zirconium and nickel phases (Fig. 8d).

For the reduced by redox-cycling cermet which was undergone aging in an environment with a low content of water vapor (variant 6), Young's modulus and strength levels are close to those for variants 2 and 4 (Tab. 2, Fig. 4a), but its fracture toughness is slightly lower compared to that of both these variants. Such a decrease in this characteristic is primarily due to the 75% lower microhardness than of the as-sintered ceramics (Fig. 4b), which in turn is caused by the

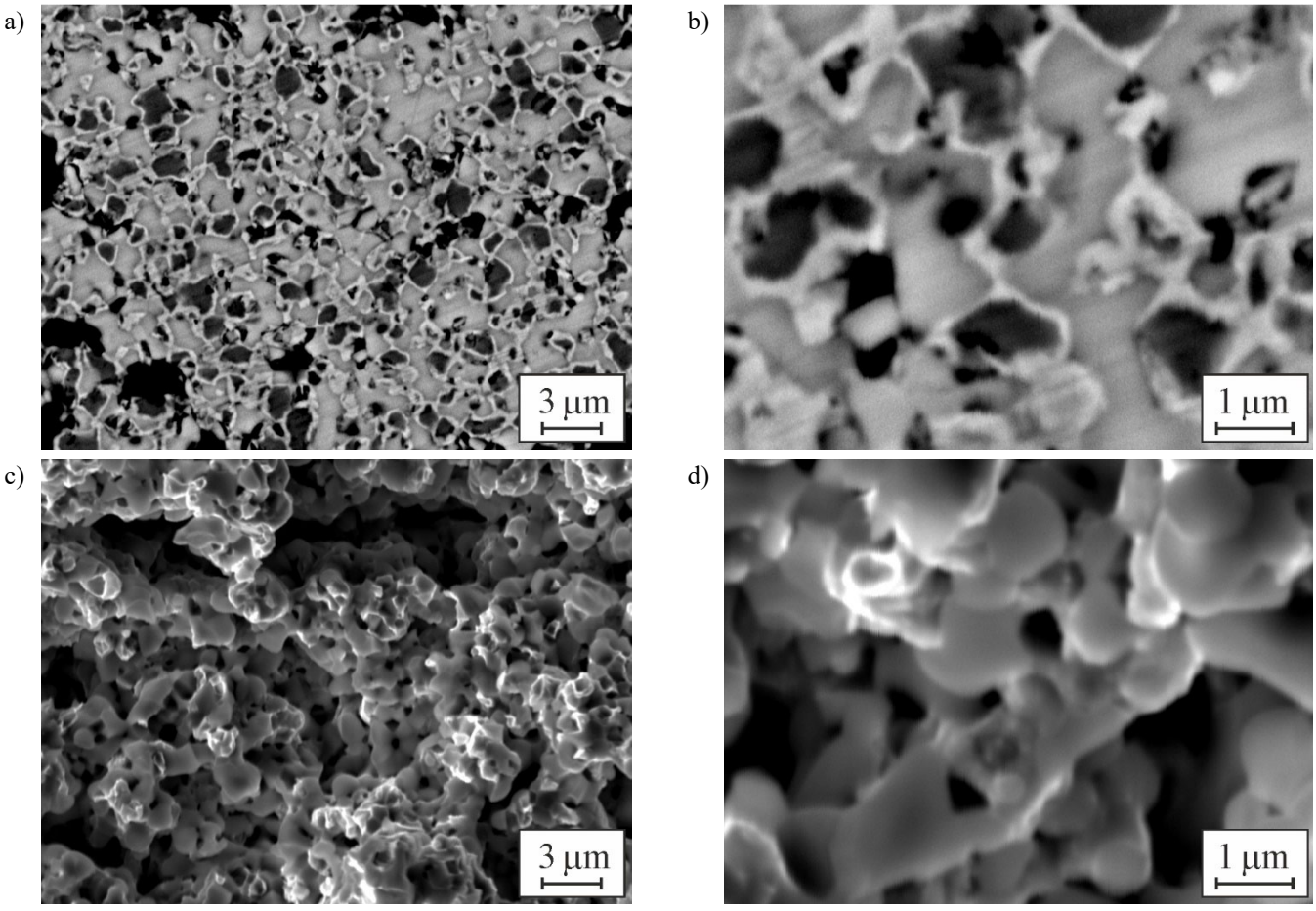

Fig. 8. SEM (a, b) microstructures (BSD images) and (c, d) fractography (SE images) of the material of variant 5 at (a, c) low and (b, d) high magnifications

Table 4.
Data of EDX spectra 1 and 2 of the YSZ–NiO(Ni) cermet specimen preconditioned with redox-cycling. The spectra correspond to areas 1 and 2, indicated by black numbered arrows in Fig. 9b

Chemical element and X-ray series	Spectrum 1		Spectrum 2	
	wt.%	at%	wt.%	at%
O K	26.03	65.42	12.63	38.06
Ni K	7.86	5.38	53.67	44.08
Y L	4.99	2.26	2.65	1.43
Zr L	61.12	26.94	31.06	16.42

degradation of the material microstructure under these conditions.

Similar to the microstructural changes due to redox treatment of the material described in the work [39], we obtained a microstructure representing the grains of the nickel phase (Fig. 9b, zone 2; Tab. 4, spectrum 2) distributed in the ceramic matrix of zirconium dioxide (Fig. 9b, zone 1; Tab. 4, spectrum 1), which became smaller compared to those in the one-time reduced material (Fig. 6b). The smaller ones have been completely reduced to metallic nickel, and the larger ones still have an unreduced core.

There are two possible reasons for the decrease in the grain size of the nickel phase [39]: (1) shrinkage, i.e. a significant decrease in the volume of the nickel phase during NiO to Ni conversion [16,59,60]; (2) diffusion of Ni^{2+} cations in half-cycles of oxidation at 600°C [13, 61-64] and, accordingly, redistribution of nickel in the bulk of the material. Since the grains contact each other with nickel fringes and thus form an electrically conductive network, this explains the higher electrical conductivity of the material after redox cycling compared to one-time reduced [42,65,66].

The microstructure of redox-cycled cermet before aging in a water vapor containing atmosphere was characterized at the meso-level by increased porosity with fragments of the network of united pores [39,62,65], and thus improved ability to pass the operating environment in the direction of localization of fuel oxidation reaction. This improvement in the functional properties of the material was not accompanied by a significant decrease in its strength as compared to the as-sintered ceramics, and in comparison with the one-time reduced material, on the contrary, it became higher. Despite the increased porosity, the cermet showed fracture toughness not lower than that of the one-time reduced material [39]. The micromechanism of fracture

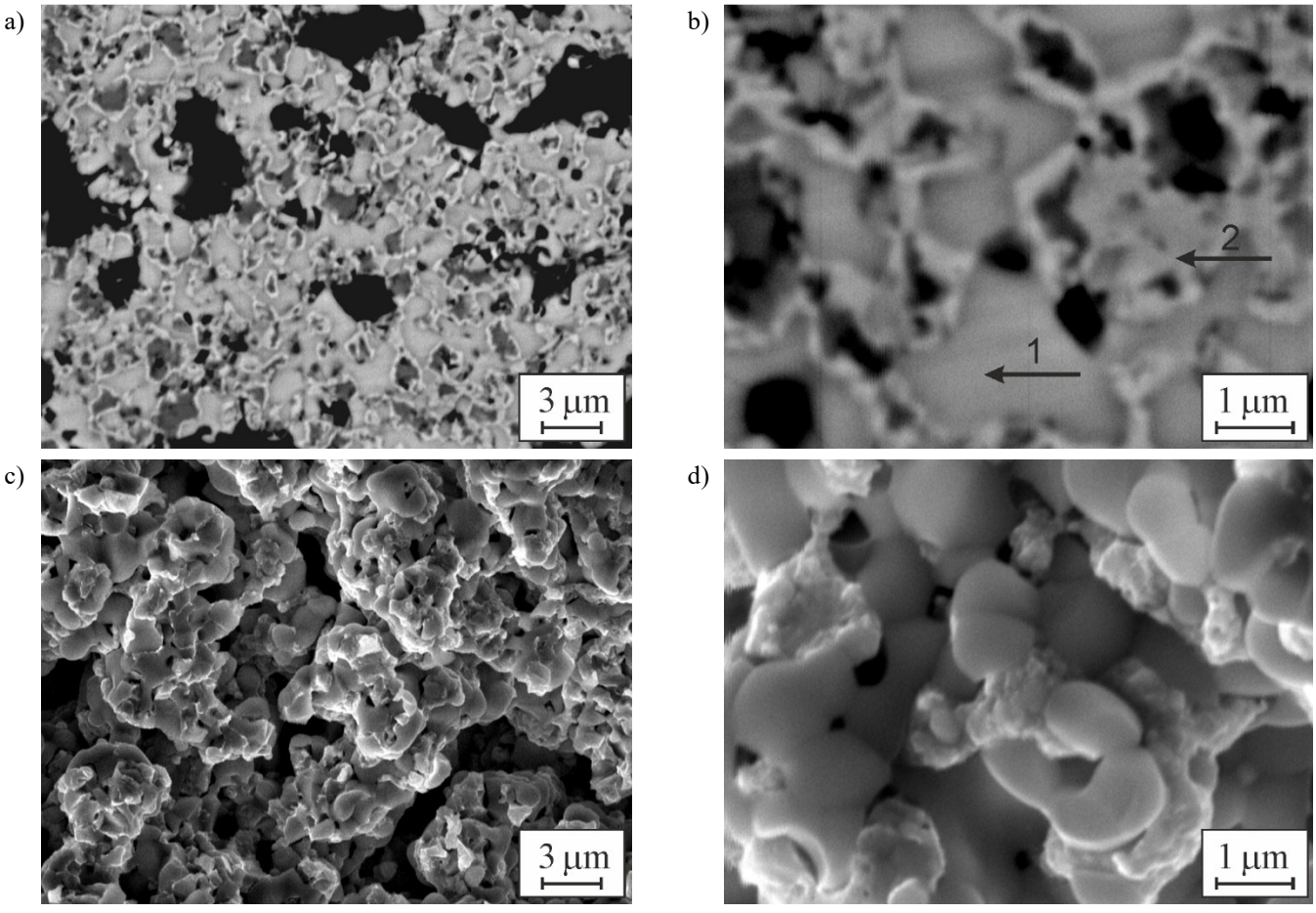

Fig. 9. SEM (a, b) microstructures (BSD images) and (c, d) fractography (SE images) of specimens preconditioned by redox treatment for five cycles in Ar–5 vol% H_2 mixture and air with final reduction in Ar–5 vol% H_2 mixture, at (a, c) low and (b, d) high magnifications. Black numbered arrows indicate EDX analysis areas (see Tab. 4)

along the agglomerate boundaries is involved here, combined with a small number of microregions of plastically elongated metallic nickel (Fig. 9c, d). When microcracks come into contact with particles of a ductile metallic nickel phase, stresses relax [13,60] and the so-called mechanism of "bridging by bonds or fibers" is implemented, known as one of the ways to increase the fracture toughness of brittle materials [67-70]. The relief fracture surface (Fig. 9c, d) indicates that the crack in the process of growth bypasses such strengthened agglomerates of particles and propagates along a curved trajectory.

However, the positive effect of redox treatment of the material is levelled due to aging in an environment with low water vapor content (variant 6). The microstructure of aged material differs from other variants because in larger grains the core of unreduced nickel oxide is divided into several fragments by a chain of nanopores (Fig. 10a, b). This is probably due to the relatively rapid disintegration of the subnanoporous structure previously formed by redox-cycling [62,71]. Disintegration is facilitated by the high pressure of the environment in the local volumes of nanopores, and the presence of water vapor accelerates this process [7,12,18,72]. Such damages slightly affect the strength and Young's modulus of the material and do not cause a decrease in its electrical conductivity (Tab. 2). However, they cause the effect of "subsidence" during indentation by the Vickers pyramid [51,73], resulting in low microhardness of the material (Fig. 4b). On the fracture surface of the material specimen, we observe a fracture micromechanism (Fig. 10c, d), similar to that for variant 4 (Fig. 7c, d). The significant decrease in porosity, the level of which (Tab. 2) is calculated by the method [47], can probably be explained by the formation of multiple nanopores, which are not taken into account when calculating porosity, and thus partial closure of large pores, which are taken into account.

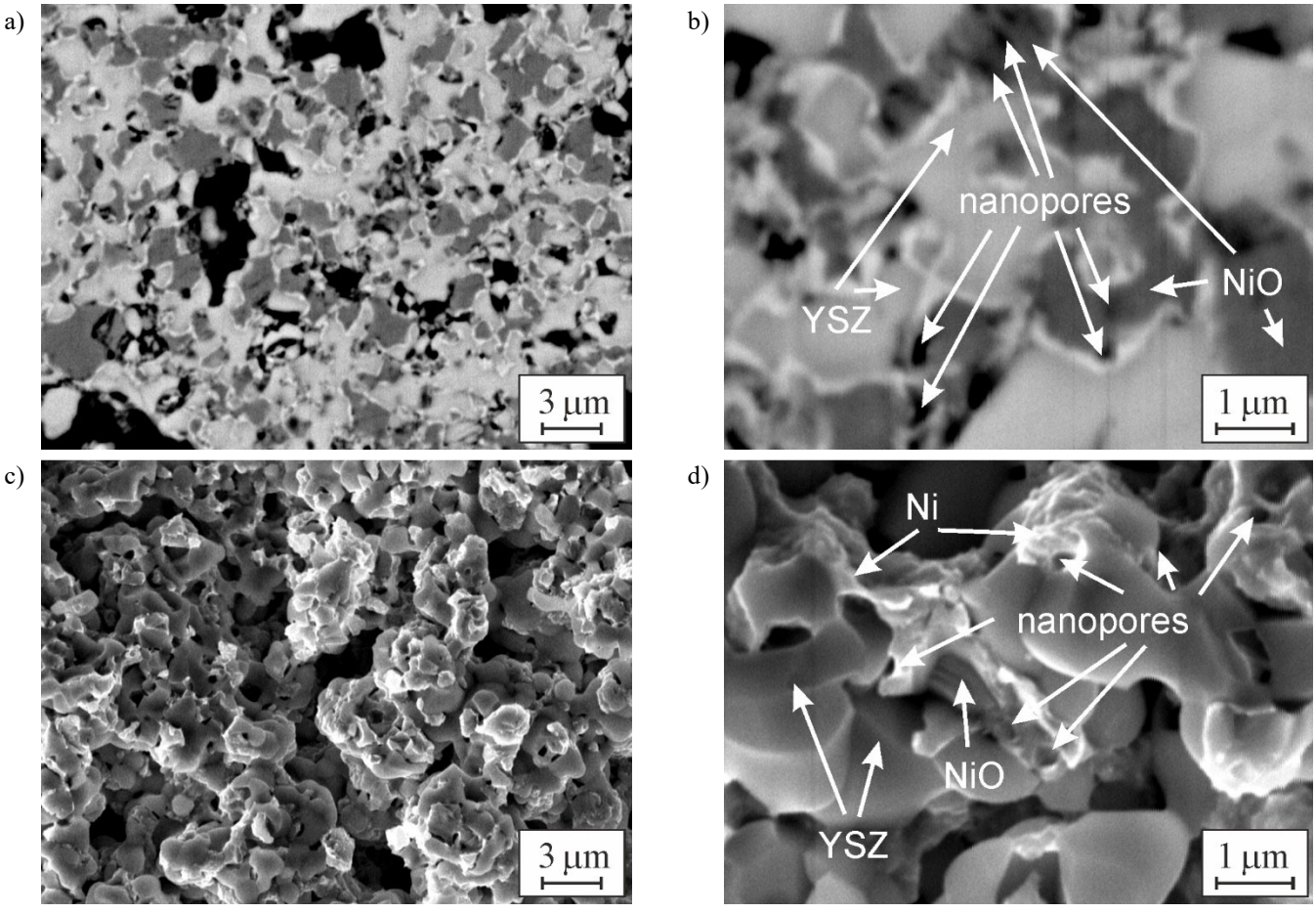

Fig. 10. SEM (a, b) microstructures (BSD images) and (c, d) fractography (SE images) of the material of variant 6 at (a, c) low and (b, d) high magnifications

As in the previous variant, the positive effect of the redox treatment of the material is levelled due to aging in a water vapor-enriched environment (variant 7). In the microstructure image of this material, we also observe in large grains of the nickel phase a core of non-reduced nickel oxide divided into several fragments by a chain of nanopores (Fig. 11a, b). However, in the presence of high-pressure water vapor, the reduced fringes of the nickel phase particles [59,60,74] were reoxidized with the formation of porous NiO nanofilms, which is observed as swelling of the fringes (Fig. 11a, b). This swelling of the fringes caused a significant reduction in the porosity of the material (Tab. 2). These processes in the material bulk caused the degradation of YSZ–NiO(Ni) cermet by debonding of small particles of the nickel phase [4,7,44,46,75] and the formation of microcracks along the grain boundaries (Fig. 11c, d). On the fracture surface of the material specimen, we observe the intergranular fracture micromechanism due to the weakening of the cohesive strength of the bonds between the zirconium and nickel phases (Fig. 11d). As a result of such structural transformations, the electrical conductivity of the cermet decreased slightly (Tab. 2). The fracture toughness and microhardness of this cermet are lower by 30.7% and 58%, respectively (Fig. 4b), and the strength and Young's modulus are lower by 33% and 28% (Tab. 2, Fig. 4a) compared to the as-sintered ceramics.

The behaviour of the material of variants 5 and 7 (pH_2O = 1.48×10^5 Pa) is a "classic" result of reoxidation [5,60,72,75]. On the one hand, compared to the material of variants 4 and 6 (pH_2O = 3.0×10^4 Pa), we observe higher levels of microhardness and fracture toughness (Fig. 4b, dependences 3 and 4, respectively). On the other hand, the lower levels of Young's modulus and flexural strength can be observed (Fig. 4a, dependences 1 and 2, respectively). Higher microhardness (Fig. 4b, dependence 3), obviously, is a consequence of the reoxidation of thin fringes of metallic

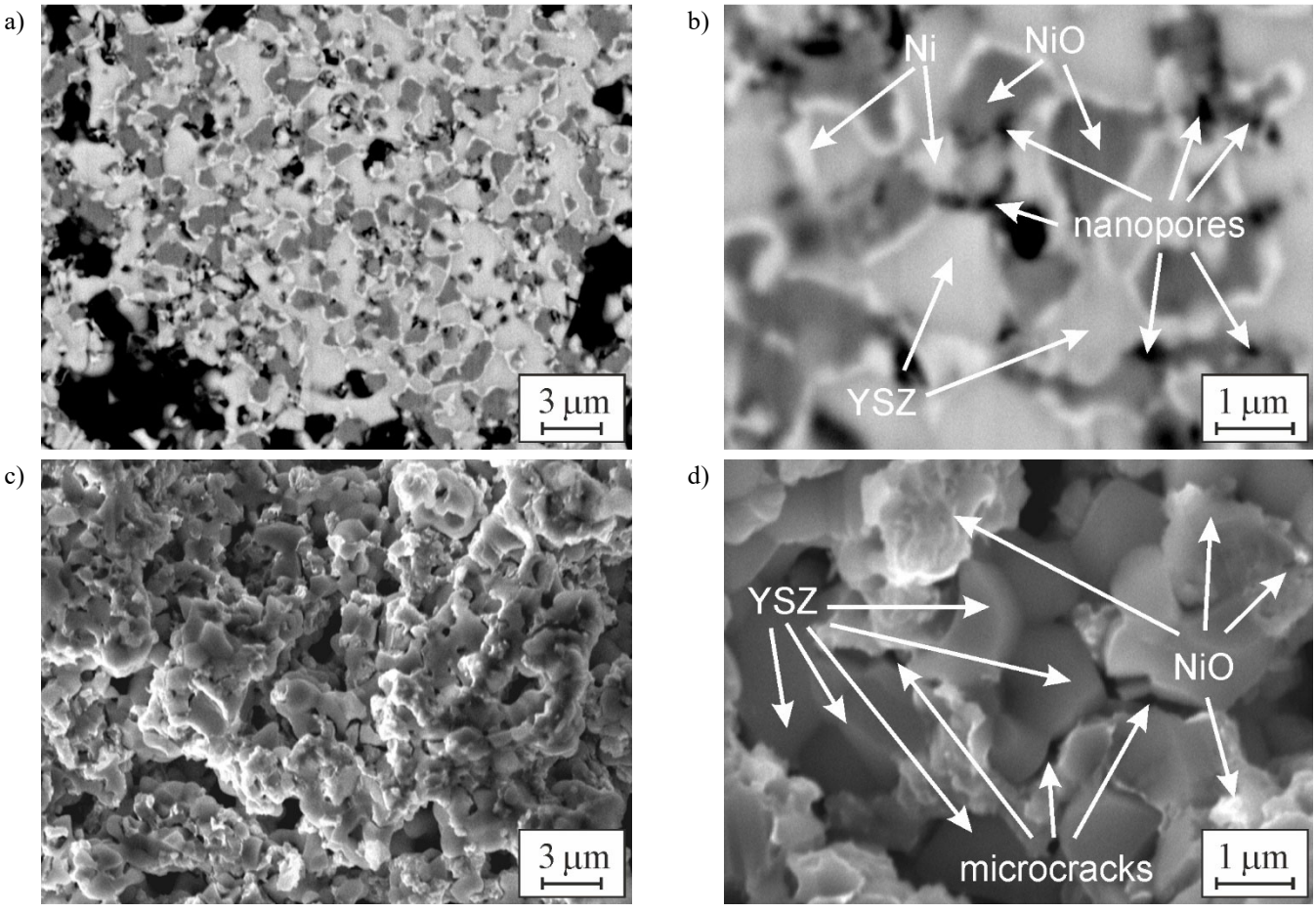

Fig. 11. SEM (a, b) microstructures (BSD images) and (c, d) fractography (SE images) of the material of variant 7 at (a, c) low and (b, d) high magnifications

nickel formed on the surfaces of the nickel phase particles during the preconditioning process, both by one-time reduction and redox-cycling [60]. This, in turn, affects the level of fracture toughness, but to a lesser extent (Fig. 4b, dependence 4). The negative effect of high water vapor content is reflected on a larger scale in the flexural strength, whereas in Young's modulus it is reflected weaker (Fig. 4a, dependences 2 and 1, respectively).

4. Conclusions

1. It has been shown that the fracture toughness of the YSZ–NiO(Ni) material for SOFC anodes is a characteristic that is more sensitive to microstructural changes occurring under the action of water vapor of different partial pressures in a hydrogen-containing gas environment, compared to its strength.
2. For each of the studied aging modes the conditions for the reduction and oxidation of the phases present in corresponding modifications of the material have been evaluated.
3. It was found that water vapor at its significant partial pressure in the operating environment of a SOFC causes oxidation of the surfaces of the nickel phase particles. This, in turn, causes degradation of the material due to the swelling of the fringes on these particles, their debonding from the ceramic skeleton of the zirconium phase, and loss of the integrity of the SOFC anode material. However, in the operating environment of a SOFC at a low partial pressure of water vapor, on the contrary, a process of reduction of the nickel phase particles takes place while maintaining satisfactory levels of strength and crack growth resistance of the anode material.

References

[1] J. Milewski, J. Kupecki, A. Szczęśniak, N. Uzunow, Hydrogen production in solid oxide electrolyzers coupled with nuclear reactors, International Journal of Hydrogen Energy (2020) (in press). DOI: https://doi.org/10.1016/j.ijhydene.2020.11.217

[2] A. Szczęśniak, J. Milewski, Ł. Szabłowski, W. Bujalski, O. Dybiński, Dynamic model of a molten carbonate fuel cell 1 kW stack, Energy 200 (2020) 117442. DOI: https://doi.org/10.1016/j.energy.2020.117442

[3] W.Z. Zhu, S.C. Deevi, A review on the status of anode materials for solid oxide fuel cells, Materials Science and Engineering: A 362/1-2 (2003) 228-239. DOI: https://doi.org/10.1016/S0921-5093(03)00620-8

[4] G. Brus, H. Iwai, J.S. Szmyd, An anisotropic microstructure evolution in a solid oxide fuel cell anode, Nanoscale Research Letters 15 (2020) 3. DOI: https://doi.org/10.1186/s11671-019-3226-1

[5] A. Sciazko, T. Shimura, Y. Komatsu, N. Shikazono, Ni-GDC and Ni-YSZ electrodes operated in solid oxide electrolysis and fuel cell modes, Journal of Thermal Science and Technology 16/1 (2021) JTST0013. DOI: https://doi.org/10.1299/jtst.2021jtst0013

[6] L.A. Dobrzański, L.B. Dobrzański, A.D. Dobrzańska-Danikiewicz, Additive and hybrid technologies for products manufacturing using powders of metals, their alloys and ceramics, Archives of Materials Science and Engineering 102/2 (2020) 59-85. DOI: https://doi.org/10.5604/01.3001.0014.1525

[7] Z. Jiao, N. Shikazono, N. Kasagie, Study on degradation of solid oxide fuel cell with pure Ni anode, ECS Transactions 35/1 (2011) 1735-1742. DOI: https://doi.org/10.1149/1.3570161

[8] V.G. Efremenko, Yu.G. Chabak, A. Lekatou, A.E. Karantzalis, A.V. Efremenko, High-temperature oxidation and decarburization of 14.55 wt pct Cr-cast iron in dry air atmosphere, Metallurgical and Materials Transactions A 47A/2 (2016) 1529-1543. DOI: https://doi.org/10.1007/s11661-016-3336-7

[9] S. Primdahl, Nickel/yttria-stabilised zirconia cermet anodes for solid oxide fuel cells, PhD Thesis, University of Twente, Denmark, 1999.

[10] B.D. Vasyliv, A procedure for the investigation of mechanical and physical properties of ceramics under the conditions of biaxial bending of a disk specimen according to the ring–ring scheme, Materials Science 45/4 (2009) 571-575. DOI: https://doi.org/10.1007/s11003-010-9215-2

[11] A. Włodarczyk-Fligier, M. Polok-Rubiniec, J. Konieczny, Thermal analysis of matrix composite reinforced with Al_2O_3 particles, Journal of Achievements in Materials and Manufacturing Engineering 100/1 (2020) 5-11. DOI: https://doi.org/10.5604/01.3001.0014.1957

[12] S. Buchaniec, A. Sciazko, M. Mozdzierz, G. Brus, A novel approach to the optimization of a solid oxide fuel cell anode using evolutionary algorithms, IEEE Access 7 (2019) 34361-34372. DOI: https://doi.org/10.1109/ACCESS.2019.2904327

[13] A. Faes, A. Hessler-Wyser, A. Zryd, J. Van herle, A review of RedOx cycling of solid oxide fuel cells anode, Membranes 2/3 (2012) 585-664. DOI: https://doi.org/10.3390/membranes2030585

[14] I. Danilenko, G. Lasko, I. Brykhanova, V. Burkhovetski, L. Ahkhozov, The peculiarities of structure formation and properties of zirconia-based nanocomposites with addition of Al_2O_3 and NiO, Nanoscale Research Letters 12 (2017) 125. DOI: https://doi.org/10.1186/s11671-017-1901-7

[15] B.D. Vasyliv, Improvement of the electric conductivity of the material of anode in a fuel cell by the cyclic redox thermal treatment, Materials Science 46/2 (2010) 260-264. DOI: https://doi.org/10.1007/s11003-010-9282-4
[16] V. Podhurska, B. Vasyliv, Influence of NiO reduction on microstructure and properties of porous Ni–ZrO_2 substrates, Proceedings of the 2012 IEEE International Conference on Oxide Materials for Electronic Engineering (OMEE), Lviv, 2012, 293-294. DOI: https://doi.org/10.1109/OMEE.2012.6464761
[17] M. Radovic, E. Lara-Curzio, Mechanical properties of tape cast nickel-based anode materials for solid oxide fuel cells before and after reduction in hydrogen, Acta Materialia 52/20 (2004) 5747-5756. DOI: https://doi.org/10.1016/j.actamat.2004.08.023
[18] M. Pihlatie, A. Kaiser, M. Mogens Mogensen, Mechanical properties of NiO/Ni–YSZ composites depending on temperature, porosity and redox cycling, Journal of the European Ceramic Society 29/9 (2009) 1657-1664. DOI: https://doi.org/10.1016/j.jeurceramsoc.2008.10.017
[19] Y. Komatsu, A. Sciazko, N. Shikazono, Isostatic pressing of screen printed nickel-gadolinium doped ceria anodes on electrolyte-supported solid oxide fuel cells, Journal of Power Sources 485 (2021) 229317. DOI: https://doi.org/10.1016/j.jpowsour.2020.229317
[20] ASTM E 384-11. Standard test method for Knoop and Vickers hardness of materials, ASTM International, 2011. DOI: https://doi.org/10.1520/E0384-11
[21] ASTM C 1327-03. Standard test method for Vickers indentation hardness of advanced ceramics, ASTM International, 2003.
[22] V.G. Efremenko, Yu.G. Chabak, K. Shimizu, A.G. Lekatou, V.I. Zurnadzhy, A.E. Karantzalis, H. Halfa, V.A. Mazur, B.V. Efremenko, Structure refinement of high-Cr cast iron by plasma surface melting and post-heat treatment, Materials and Design 126 (2017) 278-290. DOI: https://doi.org/10.1016/j.matdes.2017.04.022
[23] M. Kujawa, R. Suwak, L.A. Dobrzański, A. Gerle, B. Tomiczek, Thermal characterization of halloysite materials for porous ceramic preforms, Archives of Materials Science and Engineering 107/1 (2021) 5-15. DOI: https://doi.org/10.5604/01.3001.0014.8189
[24] B.R. Lawn, M.V. Swain, Microfracture beneath point indentations in brittle solids, Journal of Materials Science 10/1 (1975) 113-122. DOI: https://doi.org/10.1007/BF00541038
[25] B.R. Lawn, E.R. Fuller, Equilibrium penny-like cracks in indentation fracture, Journal of Materials Science 10/12 (1975) 2016-2024. DOI: https://doi.org/10.1007/BF00557479
[26] A.G. Evans, E.A. Charles, Fracture toughness determinations by indentation, Journal of the American Ceramic Society 59/7-8 (1976) 371-372. DOI: https://doi.org/10.1111/j.1151-2916.1976.tb10991.x
[27] K. Tanaka, Elastic/plastic indentation hardness and indentation fracture toughness: The inclusion core model, Journal of Materials Science 22/4 (1987) 1501-1508. DOI: https://doi.org/10.1007/BF01233154
[28] K. Niihara, R. Morena, D.P.H. Hasselman, Evaluation of K_{Ic} of brittle solids by the indentation method with low crack-to-indent ratios, Journal of Materials Science Letters 1/1 (1982) 13-16. DOI: https://doi.org/10.1007/BF00724706
[29] K. Niihara, A fracture mechanics analysis of indentation-induced Palmqvist crack in ceramics, Journal of Materials Science Letters 2/5 (1983) 221-223. DOI: https://doi.org/10.1007/BF00725625
[30] I. Danilenko, F. Glazunov, T. Konstantinova, I. Yashchyshyn, V. Burkhovetski, G. Volkova, Effect of Ni/NiO particles on structure and crack propagation in zirconia based composites, Advanced Materials Letters 5/8 (2014) 465-471. DOI: https://doi.org/10.5185/amlett.2014.amwc1040II
[31] O.N. Grigoriev, V.B. Vinokurov, T.V. Mosina, L.M. Melakh, N.D. Bega, A.V. Koroteev, L.I. Klimenko, A.V. Stepanenko, Kinetics of shrinkage, structurization, and the mechanical characteristics of zirconium boride sintered in the presence of activating additives, Powder Metallurgy and Metal Ceramics 55/11-12 (2017) 676-688. DOI: https://doi.org/10.1007/s11106-017-9855-y
[32] G.A. Gogotsi, S.N. Dub, E.E. Lomonova, B.I. Ozersky, Vickers and Knoop indentation behaviour of cubic and partially stabilized zirconia crystals, Journal of the European Ceramic Society 15/5 (1995) 405-413. DOI: https://doi.org/10.1016/0955-2219(95)91431-M
[33] O.P. Ostash, V.V. Kulyk, T.M. Lenkovskiy, Z.A. Duriagina, V.V. Vira, T.L. Tepla, Relationships between the fatigue crack growth resistance characteristics of a steel and the tread surface damage of railway wheel, Archives of Materials Science and Engineering 90/2 (2018) 49-55. DOI: https://doi.org/10.5604/01.3001.0012.0662
[34] M.A. Aswad, Comparison of the fracture toughness of high temperature ceramic measured by digital image correlation and indentation method, Journal of University of Babylon 22/4 (2014) 927-937.
[35] G.R. Anstis, P. Chantikul, B.R. Lawn, D.B. Marshall, A critical evaluation of indentation techniques for measuring fracture toughness: I, Direct crack measurement, Journal of the American Ceramic Society 64/9 (1981) 533-538. DOI: https://doi.org/10.1111/j.1151-2916.1981.tb10320.x
[36] B.R. Lawn, A.G. Evans, D.B. Marshall, Elastic/plastic indentation damage in ceramics: The median/radial crack system, Journal of the American Ceramic Society 63/9-10 (1980) 574-581. DOI: https://doi.org/10.1111/j.1151-2916.1980.tb10768.x
[37] J.E. Blendell, The origins of internal stresses in polycrystalline alumina and their effects on mechanical properties, Cambridge, 1979.

[38] J. Lankford, Indentation microfracture in the Palmqvist crack regime: implications for fracture toughness evaluation by the indentation method, Journal of Materials Science Letters 1/11 (1982) 493-495. DOI: https://doi.org/10.1007/BF00721938
[39] B. Vasyliv, V. Kulyk, Z. Duriagina, D. Mierzwinski, T. Kovbasiuk, T. Tepla, Estimation of the effect of redox treatment on microstructure and tendency to brittle fracture of anode materials of YSZ–NiO(Ni) system, Eastern-European Journal of Enterprise Technologies 108/6(12) (2020) 67-77. DOI: https://doi.org/10.15587/1729-4061.2020.218291
[40] M. Spyrka, R. Atraszkiewicz, L. Klimek. A new ceramic composite based on spherical aluminium oxide for auxiliary panels in high-temperature firing processes, Archives of Materials Science and Engineering 101/1 (2020) 5-14. DOI: https://doi.org/10.5604/01.3001.0013.9501
[41] L.A. Dobrzański, L.B. Dobrzański, A.D. Dobrzańska-Danikiewicz, Manufacturing technologies thick-layer coatings on various substrates and manufacturing gradient materials using powders of metals, their alloys and ceramics, Journal of Achievements in Materials and Manufacturing Engineering 99/1 (2020) 14-41. DOI: https://doi.org/10.5604/01.3001.0014.1598
[42] D. Waldbillig, A. Wood, D.G. Ivey, Electrochemical and microstructural characterization of the redox tolerance of solid oxide fuel cell anodes, Journal of Power Sources 145/2 (2005) 206-215. DOI: https://doi.org/10.1016/j.jpowsour.2004.12.071
[43] B.D. Vasyliv, V.Ya. Podhurska, O.P. Ostash, V.V. Vira, Effect of a hydrogen sulfide-containing atmosphere on the physical and mechanical properties of solid oxide fuel cell materials, in: O. Fesenko, L. Yatsenko (eds.), Nanochemistry, Biotechnology, Nanomaterials, and Their Applications. NANO 2017. Springer Proceedings in Physics, Vol. 214, Springer, Cham, 2018, 475-485. DOI: https://doi.org/10.1007/978-3-319-92567-7_30
[44] L.Ya. Ropyak, M.V. Makoviichuk, I.P. Shatskyi, I.M. Pritula, L.O. Gryn, V.O. Belyakovskyi, Stressed state of laminated interference-absorption filter under local loading, Functional Materials 27/3 (2020) 638-642. DOI: https://doi.org/10.15407/fm27.03.638
[45] V.M. Posuvailo, V.V. Kulyk, Z.A. Duriagina, I.V. Koval'chuck, M.M. Student, B.D. Vasyliv, The effect of electrolyte composition on the plasma electrolyte oxidation and phase composition of oxide ceramic coatings formed on 2024 aluminium alloy, Archives of Materials Science and Engineering 105/2 (2020) 49-55. DOI: https://doi.org/10.5604/01.3001.0014.5761
[46] T.S. Cherepova, H.P. Dmytrieva, O.I. Dukhota, M.V. Kindrachuk, Properties of nickel powder alloys hardened with titanium carbide, Materials Science 52/2 (2016) 173-179. DOI: https://doi.org/10.1007/s11003-016-9940-2
[47] I.B. Ivasenko, V.M. Posuvailo, M.D. Klapkiv, V.A. Vynar, S.I. Ostap'yuk, Express method for determining the presence of defects of the surface of oxide-ceramic coatings, Materials Science 45/3 (2009) 460-464. DOI: https://doi.org/10.1007/s11003-009-9191-6
[48] T.B. Reed, Free energy of formation of binary compounds, MIT Press, Cambridge, 1971.
[49] Z. Peng, J. Gong, H. Miao, On the description of indentation size effect in hardness testing for ceramics: Analysis of the nanoindentation data, Journal of the European Ceramic Society 24/8 (2004) 2193-2201. DOI: https://doi.org/10.1016/S0955-2219(03)00641-1
[50] I.M. Spiridonova, E.V. Sukhovaya, S.B. Pilyaeva, O.G. Bezrukavaya, The use of composite coatings during metallurgical equipment parts repair, Metallurgicheskaya i Gornorudnaya Promyshlennost 3 (2002) 58-61.
[51] L.Ya. Ropyak, I.P. Shatskyi, M.V. Makoviichuk, Influence of the oxide-layer thickness on the ceramic-aluminium coating resistance to indentation, Metallofizika i Noveishie Tekhnologii, 39/4 (2017) 517-524. DOI: https://doi.org/10.15407/mfint.39.04.0517
[52] J.W. Adams, R. Ruh, K.S. Mazdiyasni, Young's modulus, flexural strength, and fracture of yttria-stabilized zirconia versus temperature, Journal of the American Ceramic Society 80/4 (1997) 903-908. DOI: https://doi.org/10.1111/j.1151-2916.1997.tb02920.x
[53] R.F. Cook, G.M. Pharr, Direct observation and analysis of indentation cracking in glasses and ceramics, Journal of the American Ceramic Society, 73/4 (1990) 787-817. DOI: https://doi.org/10.1111/j.1151-2916.1990.tb05119.x
[54] A. Nastic, A. Merati, M. Bielawski, M. Bolduc, O. Fakolujo, M. Nganbe, Instrumented and Vickers indentation for the characterization of stiffness, hardness and toughness of zirconia toughened Al_2O_3 and SiC armor, Journal of Materials Science and Technology 31/8 (2015) 773-783. DOI: https://doi.org/10.1016/j.jmst.2015.06.005
[55] P. Kim, D. Brett, N. Brandon, The effect of water content on the electrochemical impedance response and microstructure of Ni-CGO anodes for solid oxide fuel cells, Journal of Power Sources 189/2 (2009) 1060-1065. DOI: https://doi.org/10.1016/j.jpowsour.2008.12.150
[56] B.R. Lawn, Fracture of brittle solids, Second Edition, Cambridge University Press, Cambridge, 1993. DOI: https://doi.org/10.1017/CBO9780511623127
[57] P. Khajavi, P.V. Hendriksen, J. Chevalier, L. Gremillard, H.L. Frandsen, Improving the fracture toughness of stabilized zirconia-based solid oxide cells fuel electrode supports: Effects of type and concentration of stabilizer(s), Journal of the European

Ceramic Society 40/15 (2020) 5670-5682. DOI: https://doi.org/10.1016/j.jeurceramsoc.2020.05.042
[58] H.A. Shabri, M.H.D. Othman, M.A. Mohamed, T.A. Kurniawan, S.M. Jamil, Recent progress in metal-ceramic anode of solid oxide fuel cell for direct hydrocarbon fuel utilization: A review, Fuel Processing Technology 212 (2021) 106626. DOI: https://doi.org/10.1016/j.fuproc.2020.106626
[59] T. Utigard, M. Wu, G. Plascencia, T. Marin, Reduction kinetics of Goro nickel oxide using hydrogen, Chemical Engineering Science 60/7 (2005) 2061-2068. DOI: https://doi.org/10.1016/j.ces.2004.11.024
[60] A. Faes, A. Nakajo, A. Hessler-Wyser, D. Dubois, A. Brisse, S. Modena, J. Van Herle, RedOx study of anode-supported solid oxide fuel cell, Journal of Power Sources 193/1 (2009) 55-64. DOI: https://doi.org/10.1016/j.jpowsour.2008.12.118
[61] J.G. Railsback, A.C. Johnston-Peck, J. Wang, J.B. Tracy, Size-dependent nanoscale Kirkendall efect during the oxidation of nickel nanoparticles, ACS Nano 4/4 (2010) 1913-1920. DOI: https://doi.org/10.1021/nn901736y
[62] Ye. Kharchenko, Z. Blikharskyy, V. Vira, B. Vasyliv, V. Podhurska, Study of nanostructural changes in a Ni-containing cermet material during reduction and oxidation at 600°C. Applied Nanoscience 10/12 (2020) 4535-4543. DOI: https://doi.org/10.1007/s13204-020-01391-1
[63] X.W. Zhou, Y.F. Shen, H.M. Jin, Effect of deposition mechanism and microstructure of nano-ceria oxide addition on Ni-P coating by pulse electrodeposition, Advanced Materials Research 326 (2011) 151-156. DOI: https://doi.org/10.4028/www.scientific.net/AMR.326.151
[64] I.M. Andreiko, V.V. Kulyk, O.P. Ostash, Resistance of steels of railroad wheels to corrosion-fatigue fracture, Materials Science 47/5 (2012) 608-612. DOI: https://doi.org/10.1007/s11003-012-9434-9
[65] A. Wood, D. Waldbillig, Preconditioning treatment to enhance redox tolerance of solid oxide fuel cells, US Patent 8,029,946 B2, 2011.
[66] B. Vasyliv, J. Milewski, V. Podhurska, T. Wejrzanowski, V. Kulyk, J. Skibiński, V. Vira, Ł. Szabłowski, A. Szczęśniak, O. Dybiński, Study of the degradation of a fine-grained YSZ–NiO anode material during reduction in hydrogen and reoxidation in air, Applied Nanoscience (2021) (published online). DOI: https://doi.org/10.1007/s13204-021-01768-w
[67] T. Sung Oh, R.M. Cannon, R.O. Ritchie, Subcritical crack growth along ceramic-metal interfaces, Journal of the American Ceramic Society 70/12 (1987) C-352-C-355. DOI: https://doi.org/10.1111/j.1151-2916.1987.tb04917.x
[68] O.V. Sukhova, Influence of mechanisms of structure formation of interfaces in composites on their properties, Metallofizika i Noveishie Tekhnologii 31/7 (2009) 1001-1012.
[69] O.P. Ostash, V.H. Anofriev, I.M. Andreiko, L.A. Muradyan, V.V. Kulyk, On the concept of selection of steels for high-strength railroad wheels, Materials Science 48/6 (2013) 697-703. DOI: https://doi.org/10.1007/s11003-013-9557-7
[70] R.O. Ritchie, Mechanisms of fatigue-crack propagation in ductile and brittle solids, International Journal of Fracture 100/1 (1999) 55-83. DOI: https://doi.org/10.1023/A:1018655917051
[71] S.S. Savka, D.I. Popovych, A.S. Serednytski, Molecular dynamics simulations of the formation processes of zinc oxide nanoclusters in oxygen environment, in: O. Fesenko, L. Yatsenko (eds.), Nanophysics, Nanomaterials, Interface Studies, and Applications. NANO 2016. Springer Proceedings in Physics, Vol. 195, Springer, Cham, 2017, 145-156. DOI: https://doi.org/10.1007/978-3-319-56422-7_11
[72] L.A. Dobrzański, L.B. Dobrzański, A.D. Dobrzańska-Danikiewicz, Overview of conventional technologies using the powders of metals, their alloys and ceramics in Industry 4.0 stage, Journal of Achievements in Materials and Manufacturing Engineering 98/2 (2020) 56-85. DOI: https://doi.org/10.5604/01.3001.0014.1481
[73] K. Buła, A. Palatyńska-Ulatowska, L. Klimek, Biodentine management and setting time with Vicat and Vickers evaluation; a survey-based study on clinicians' experience, Archives of Materials Science and Engineering 103/2 (2020) 75-85. DOI: https://doi.org/10.5604/01.3001.0014.3358
[74] B. Vasyliv, V. Podhurska, O. Ostash, Preconditioning of the YSZ–NiO fuel cell anode in hydrogenous atmospheres containing water vapor, Nanoscale Research Letters 12 (2017) 265. DOI: https://doi.org/10.1186/s11671-017-2038-4
[75] M. Szota, A. Łukaszewicz, K. Machnik, The possibility to control the thickness of the oxide layer on the titanium Grade 2 by mechanical activation and heat treatment, Journal of Achievements in Materials and Manufacturing Engineering 100/2 (2020) 70-77. DOI: https://doi.org/10.5604/01.3001.0014.3346

© 2021 by the authors. Licensee International OCSCO World Press, Gliwice, Poland. This paper is an open access paper distributed under the terms and conditions of the Creative Commons Attribution-NonCommercial-NoDerivatives 4.0 International (CC BY-NC-ND 4.0) license (https://creativecommons.org/licenses/by-nc-nd/4.0/deed.en).